

Case History

2D waveform tomography applied to long-streamer MCS data from the Scotian Slope

Matthias Delescluse¹, Mladen R. Nedimović², and Keith E. Louden³

ABSTRACT

Detailed velocity models of the earth's subsurface can be obtained through waveform tomography. The accuracy of the long-wavelength component of such velocity models, which is the background velocity field, is particularly sensitive to modeling low-frequency refracted waves that have long paths through target structures. Thus, field examples primarily have focused on the analysis of long-offset wide-angle data sets collected using autonomous receivers, in which refractions arrive at significantly earlier times than reflections. Modern marine acquisition with long streamers now offers the ability to record refracted waves with high spatial density and uniform source, both in shallow and deep water. We used 2D multichannel seismic (MCS) data acquired with a 9-km-long streamer over the Scotian Slope in water depths of ~1600 m. The refracted arrivals, although mostly restricted to far-offset receivers, provided sufficient information to successfully invert for a high-

resolution background velocity field. Using a frequency-domain acoustic code over frequencies from 8 to 24 Hz on two crossing profiles, we found that the limited refracted waves can constrain the velocity field above the depth of the turning waves (~1.5 km below seafloor). Several important features were resolved by the waveform velocity model that were not present in the initial traveltimes model. In particular, a high-velocity layer at 300 m below the seafloor, interpreted as gas hydrates, was imaged even where a characteristic bottom-simulating reflector was not visible. At 750-m depth, a strong velocity increase of 300 m/s existed beneath a gently dipping reflector along which low-velocity zones, possibly related to gas, were present. Velocity models were highly consistent at the crossing point between the two profiles. The depth extent of the MCS waveform tomography constrained by refractions could be extended by even longer streamers (e.g., 15 km) or by joint inversion with data from ocean-bottom seismographs.

INTRODUCTION

Applications of frequency-domain 2D acoustic waveform tomography inversion (Pratt and Worthington, 1990; Pratt, 1999) to field seismic data are few and limited to the two end-members of seismic-acquisition techniques: (1) long-offset wide-angle refraction experiments using individual land or ocean-bottom stations (Dessa et al., 2004; Operto et al., 2004; Ravaut et al., 2004; Operto et al., 2006; Bleibinhaus et al., 2007, 2009) and (2) high-resolution, short-streamer marine reflection seismics (Hicks and Pratt, 2001; Shin and Min, 2006; Wang and Rao,

2009). The two cases offer opposite advantages and drawbacks. In the "refraction" case, the monoparameter inversion of P-wave velocities is questionable because of attenuation variations, typically limiting the inversion to phase only (Bleibinhaus et al., 2007), whereas good starting models obtained from traveltimes tomography and low frequencies offer excellent control on the velocity field (Brenders and Pratt, 2007b). In the "reflection" case, small offsets and small-scale targets with simple structures ensure a good validity of the acoustic approximation (Barnes and Charara, 2009; Virieux and Operto, 2009), and the high density of shots and receivers allow very high resolution.

Manuscript received by the Editor 12 July 2010; revised manuscript received 2 March 2011; published online 13 June 2011.

¹Formerly Dalhousie University, Department of Oceanography, Halifax, Nova Scotia, Canada; presently, École Normale Supérieure de Paris, Laboratoire de Géologie. E-mail: delescluse@geologie.ens.fr.

²Dalhousie University, Department of Oceanography, Halifax, Nova Scotia, Canada; and Columbia University, Lamont-Doherty Earth Observatory, Palisades, New York, U.S.A. E-mail: mladen@dal.ca.

³Dalhousie University, Department of Oceanography, Halifax, Nova Scotia, Canada. E-mail: keith.louden@dal.ca.

© 2011 Society of Exploration Geophysicists. All rights reserved.

However, the background velocity field is not well constrained by reflection waveform tomography, and a degree of structural interpretation is necessary to obtain a useful result (Hicks and Pratt, 2001; Wang and Rao, 2009). Although fewer studies using long-offset multichannel seismic (MCS) data have been attempted, such data are increasingly available, and the applicability of the waveform inversion to these data sets needs further study (a review of industry efforts in applying waveform tomography to field data can be found in Williamson et al., 2010).

In this paper, we attempt 2D waveform tomography inversion in the frequency domain using a long-streamer MCS data set, which represents an intermediate situation between the two previously cited cases. An earlier attempt to use full waveform tomography for long-streamer data (Shipp and Singh, 2002) was done in the time-space domain, but the huge computational cost associated with this method required severe decimation of the input data, thus limiting the results.

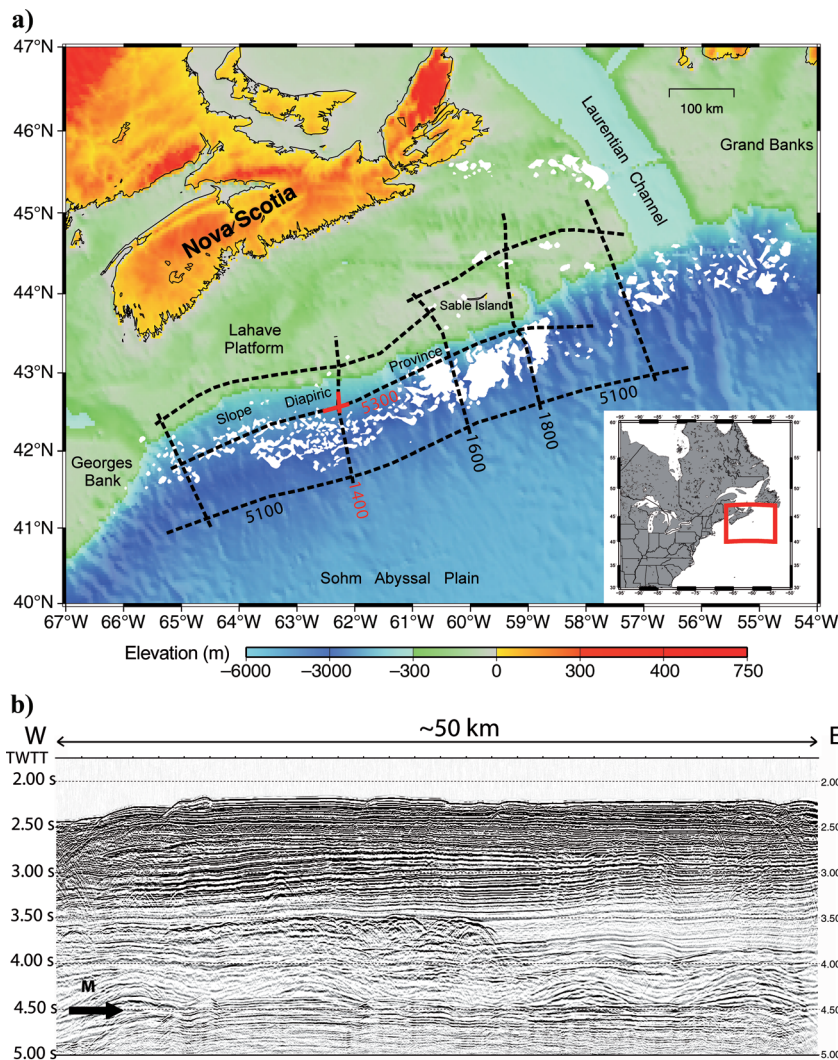


Figure 1. (a) Location of the Novaspan 2D lines acquired by GXT in 2003 on the Scotian Slope using a 9-km-long streamer (dashed lines). The inset shows the location of Nova Scotia on the east coast of North America. The crossing red sections of lines 5300 and 1400 are used in this study. White areas represent salt. (b) Stack of the section of line 5300 investigated in this study. Seafloor multiples (M) are visible. The turning depth of the recorded refraction waves is at ~ 3.5 s two-way traveltime (TWTT).

The 2D MCS data with a 9-km-long streamer were acquired on the Scotian Slope (Figure 1a) on a thick sedimentary basin formed after Mesozoic rifting between North America and Africa. The stack section along line 5300 (Figure 1b) shows subparallel layers deposited from the Pliocene in an area with known accumulations of gas hydrates and free gas (Leblanc et al., 2007). Shot gathers include refracted waves arriving earlier than the seafloor reflection and later than the direct wave (Figure 2). These waves constrain the background velocity field above their turning depth, while the simple, slowly varying sedimentary environment (Figure 1b) minimizes the limitation with the acoustic approximation. This configuration is then likely to combine the strengths of reflection and refraction cases of waveform inversion while limiting their drawbacks. We first present the method and the data set and then describe the preconditioning and inversion strategy. Finally, we discuss the results in terms of limitations of the waveform tomography method applied to MCS data, possible targets

of MCS waveform tomography, and the additional information it can provide when compared to a prestack depth-migration image.

FREQUENCY-DOMAIN WAVEFORM TOMOGRAPHY APPLIED TO MCS DATA

General method

In this section we briefly describe the waveform inversion methodology that is used. The reader can find further details in Pratt et al. (1998), or Sirgue and Pratt (2004).

The wavefield u can be defined as the solution to a set of nonlinear equations (here the frequency-domain acoustic wave equation g) depending on parameters m (the P-wave velocities in every cell of a grid):

$$g(m) = u,$$

Several possibilities exist to measure the misfit $E(m)$ between the field data and the synthetic data, such as the L1-Norm (Brossier et al., 2010), the logarithmic approach (Shin et al., 2007), or the more classical L2-Norm (Tarantola, 1987), where

$$E(m) = \frac{1}{2} \partial d^T \partial d,$$

with $\partial d = g(m) - d_{\text{obs}}$ being the difference between the forward model using parameters m and the data d_{obs} ; ∂d^T is the complex conjugate of this difference. The goal of the inversion is to find the parameters m that minimize this misfit function. To do this, we introduce the gradient of the misfit function $\nabla_m E = \partial E / \partial m$, which gives the direction of increase of the misfit in the parameter space. In the linear case, the misfit function is quadratic and can be expressed as a Taylor series of the second order. The model update ∂m is derived in the Newton method as

$$\partial m = H^{-1} \nabla_m E(m_0),$$

with H being the Hessian, $\partial(\nabla E)/\partial m$, and m_0 representing the parameters of the initial model.

In the nonlinear case the Hessian is challenging to obtain even if the misfit function is assumed to be locally linear near the model m_0 . It can be, at best, only approximated, and several iterations are necessary. If the problem is strongly nonlinear, the gradient is not in the steepest ascent direction after the first iteration, and it needs to be updated. To avoid calculating the Hessian, the gradient method is used, where

$$m^{(k)} = m^{(k-1)} - \gamma^{(k-1)} \nabla_m E^{(k-1)}.$$

With this method, the model is updated in the direction of the steepest descent and assures that the new misfit at iteration k is smaller than the misfit at iteration $k - 1$. The step-length γ has to be estimated either by a line search (which is computationally expensive) or by a new Newton calculation requiring only one new forward model where the model is perturbed in the gradient direction.

Calculating the gradient $\nabla_m E$ would normally require perturbing every parameter to compute all the partial derivatives as $\nabla_m E = J^T \partial d$, with $J_{ij} = \partial u_i / \partial m_j$ being the Fréchet derivative matrix. This approach is computationally expensive. Using the adjoint-state method, it can be shown that, instead, the gradient can be expressed as a product of the forward-propagated wavefield of the source term,

$$P_f(x, s) = G(x, s)S(\omega),$$

and the back-propagated wavefield of the residuals from the receiver location,

$$P_b(x, r, s) = G(x, r)^T \partial d(r, s).$$

$G(x, r)$ and $G(x, s)$ are Green's functions, $S(\omega)$ is the source term, and $\partial d(r, s)$ are the residuals for the source s and receiver r . Note that this gradient calculation is similar to prestack migration (Lailly, 1983; Tarantola, 1984).

In summary, three forward models are needed for each iteration: one to compute the wavefield in the initial model, another to calculate the back-propagated residuals, and a final one to compute the step length.

Field data application challenges

The success of the inversion depends on the accuracy of the starting velocity model. Because the problem is nonlinear, the gradient may point toward a local minimum. Finding a starting model that at long to intermediate wavelengths agrees with the true one is the best approach to counter the nonlinearity of the inversion and find a global minimum.

A standard method to obtain an accurate starting velocity model is to use traveltime tomography. However, streamer traveltime tomography using refracted arrivals constrains only large wavelengths of the velocity model, typically around 1 km for the shallow part and wavelengths greater than 1–2 km at depth (see Canales et al., 2008; Newman et al., 2011).

Applying waveform tomography afterward may be challenging if a gap in the intermediate wavelengths exists (see the Marmousis example in Sirgue [2003] and Shin et al. [2007]). In other words, if the lowest usable signal frequency in the data set does not cover the highest wavelength extracted by the travel-time tomography. Short-streamer reflection seismics is typically a high-frequency acquisition that will not allow the reconstruction of intermediate wavelengths (Jannane et al., 1989). Long-offset seismic data introduce nonlinearity (Sirgue, 2006) because the misfit results from the sum of the slowness error along the wave path. The longer the wave path, the more nonlinear the problem is. However, long-streamer seismic data sets provide more information on the low wavenumbers (Sirgue, 2006), which are essential to the success of waveform inversion.

To successfully invert for a velocity field, it is also essential to have a field data set that can be compared with the synthetic data produced by the finite-difference forward modeling. We summarize four main issues that need attention when comparing field and synthetic data: (1) Is the field data set significantly affected by elastic effects? This is important because we only model acoustic wave propagation. The risk is that amplitudes may not be useable. If this is the case, only the phase information of the wavefield can be used, which requires that the synthetic and field amplitudes are normalized to one. (2) Although densities and attenuation vary in the subsurface, only P-wave velocities are inverted for. This means that the constant density

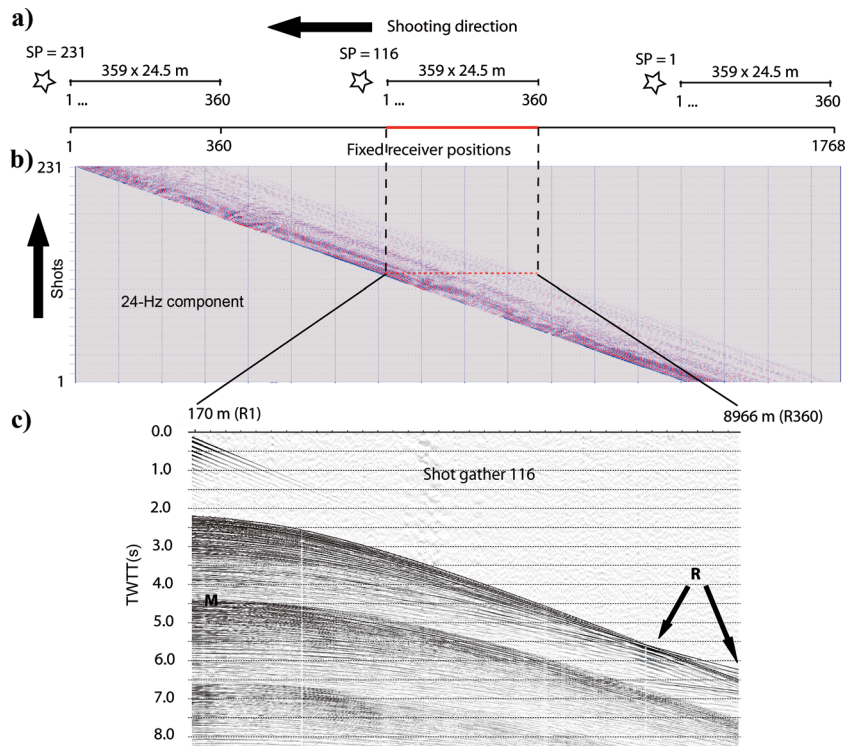


Figure 2. (a) Sketch of the streamer geometry in relation to the fixed receiver array. The active receivers for shot 116 are indicated in red. (b) Example of the frequency-domain data in a shot-receiver space. The 24-Hz component of the data is displayed, and the red dashed line indicates the 24-Hz component of the data for all 360 traces. For each shot, nonactive receivers have a zero component. (c) Shot gather 116 corresponding to the positions above. Refracted arrivals (R) arriving before the seafloor reflection are indicated as well as the first multiple of the seafloor (M).

of the subsurface used for the inversion will mostly affect the reflectivity part of the data set, with the reflectors being interpreted as pure velocity contrasts. Attenuation will affect the amplitudes if there are strong attenuation variations that are not taken into account. This last problem can also potentially require phase-only inversion even if the acoustic approximation is valid. (3) The modeled acoustic energy propagation is 2D, whereas a field data set records energy propagating in 3D. To compare the two data sets, the field data have to be corrected for cylindrical instead of spherical energy propagation. (4) The signal-to-noise ratio of the field data must be high to avoid artifacts because noise is not modeled by the acoustic code. Smoothing the gradient and using many frequencies can help reduce artifacts.

The case of an MCS data set from a simple geological framework

The intermediate wavelength problem and the other issues cited above can be minimized by applying waveform tomography to a data set acquired from a simple geological environment. The Ion-GXT data set was acquired along the Scotian Slope. This area of the slope is composed of a thick (~ 7 km), Triassic to Quaternary, postrift sedimentary section. The upper 2 km, which were modeled in our study, are composed of interbedded horizontal layers of prodeltaic mudstone, claystone, and siltstone deposited since the Miocene as a result of events such as the late Tertiary sea-level lowstands (Piper and Normark, 1989; Leblanc et al., 2007). Recent mud depositions from the last interglacial period (12 ka; Mosher et al., 1994) were cored and show soft, water-saturated seafloor properties ($V_p = 1530 \pm 20$ m/s, density = 1680 ± 50 kg/m³) (Leblanc et al., 2007). More-complex structures related to salt tectonics like diapirs (Figure 1) are too deep on line 5300 to be of concern.

This simple environment is then likely to minimize challenges during inversion for the following reasons: (1) Sudden and significant lateral variation of attenuation is not likely to occur as the sedimentary deposition system is the same over the length of the profile. (2) The S-wave velocity is likely to be slow and

smoothly increasing with depth, which will limit elastic effects. (3) Horizontal to subhorizontal layers will allow correction for the 2D instead of 3D propagation of energy. (4) It is simpler to find an accurate starting velocity model because there are no complex structures, and thus, intermediate wavelengths are minimal. Basically, we expect a 2D final model that does not differ greatly from a 1D velocity model but that still includes additional information from the inversion. These considerations will be detailed and explained in the following sections.

DATA PRECONDITIONING

Data and geometry

We use two crossing sections of the Novaspan profiles (lines 1400 and 5300; see Figure 1) acquired by Ion-GXT in 2003. The streamer is composed of 360 receiver groups with 25-m spacing. The shot spacing is 50 m. For the investigated 44-km-long section of strike line, line 5300, we decimate the data for computational reasons to 231 shots spaced every 150 m (every third shot) and use all receivers. For the crossing 29-km-long section of the dip line, line 1400, we use 196 shots spaced every 100 m (every second shot) and all receivers. Although 94 m is the ideal spacing, to avoid aliasing for our lowest frequency available (Nyquist criterion is met for an 8-Hz signal), Brenders and Pratt (2007b) show that the sampling theory criterion may be too conservative (see Table 1 for a summary of the sampling of different synthetic and real survey configurations). The impact of the data decimation is further discussed in the “Inversion Strategy” section, where we describe a test inversion of the entire, nondecimated data set for line 5300 (691 shots).

Feathering of the streamer is limited to a maximum 10° angle but is generally less. The nominal geometry implies a 170-m minimum offset for the first receiver and, consequently, a 9145-m maximum offset for receiver 360. However, streamer bending also occurs, which shortens the effective maximum offset to an average of 8966 m. To account fully for the effects of feathering and bending would be equivalent to the definition of 83,160 independent receivers positions for line 5300 (248,760 in the nondecimated line 5300) and 70,560 for line 1400 and would

Table 1. Aliasing number $N_a = 2D_{\text{samp}}f/V_{\text{min}}$ in a selection of studies involving different real and synthetic data sets. The D_{samp} column is the source or receiver interval, and V_{min} is the minimum velocity in the model. An aliasing number higher than one theoretically produces some aliasing. In practice, inversion results can be satisfactory with sparser sampling (Brenders and Pratt, 2007a).

Study	Data	Geometry	V_{min} (m/s)	D_{samp} (m)	f (Hz)	N_a
Hicks and Pratt (2001)	real	reflection	1560	12.5	10–60	0.16–1
Operto et al. (2006)	real	refraction	2000	1000	3–15	3–15
Sirgue and Pratt (2004)	synthetic	refraction	1500	100	5–10	0.7–1.3
Ravaut et al. (2004)	real	refraction	2000	90	5.4–20	0.5–1.8
Brenders and (2007b)	synthetic	refraction	4000	5000	0.8–7	2–18
Bleibinhaus et al. (2009), SAF	real	refraction	2000	500–1000	3–14	1.5–14
Bleibinhaus et al. (2009), CBI	real	refraction	1500	1000	3–16	4–21
This study, line 5300	real	MCS	1500	150	8–24	1.6–4.8
This study, line 5300 (nondecimated)	real	MCS	1500	50	8–24	0.5–1.6
This study, line 1400	real	MCS	1500	100	8–24	1.1–3.2

require 3D codes. Considering the resulting requirement for computer memory and the fact that we need to approximate our geometry to a 2D straight line, we choose to define fixed receiver positions with constant spacing that will be reused by different shots. For each shot, only 360 fixed receivers will be active (see sketch on Figure 2). In our case, an average 24.5-m spacing between receivers matches the average length of the streamer. Although the average maximum-offset length is only shortened by 2%, this is a very sensitive parameter for travel-time and waveform tomography, and it is crucial to take this shortening into account. In this respect, focusing on short sections of profiles helps to avoid potentially large changes in the geometry due to ocean currents. Finally, for line 5300, the independent receiver positions are reduced to 1768 fixed positions (Figure 2).

Amplitudes

Free-surface-related multiples (Figure 1) can be a problem in seismic data inversion if they overprint useful data. A free surface is used to compute the synthetic data so that the multiples are modeled. The frequency-domain code requires using a damping factor to remove late phases that cannot be modeled in the inversion. For wide-angle refraction studies, this is particularly useful for removing S-converted phases. In our case, we damp arrivals later than 2.5 s in our 4-s-long traces (having applied a 2000-m/s reduced velocity), which includes damping of the multiple. Moreover, the average seafloor depth of the investigated profiles is ~1600 m, which means that multiples are not a problem (Figure 1) because they arrive later than the turning waves and therefore are beneath the region where the velocity is constrained (Brenders and Pratt, 2007c). Thus, no multiple attenuation is applied.

Amplitude corrections, however, must be applied because the observed data are acquired with a point source, corresponding to a 3D geometrical spreading of the acoustic energy, while the acoustic forward-modeling code is 2D and assumes a line source with cylindrical spreading. In the near-offset domain and for horizontal layers, a simple correction can be applied as a function of $V_{rms}(t)\sqrt{t}$ (Wang and Rao, 2009), where V_{rms} is the rms velocity, or, more simply, just \sqrt{t} (Hicks and Pratt, 2001). However, in our case, the time t cannot be approximated as the normal incidence time, as for the formulas above. A simple solution (Ursin, 1990) is to apply an offset-dependent correction C after normal moveout (NMO) adjustment to normal incidence traveltimes, followed by reverse NMO:

$$C = V_{rms}(t) \left[t^2 + \frac{x^2}{V_{rms}(t)^2} \right]^{1/4},$$

where x is the offset, t is the normal incidence traveltimes, and the propagation medium is assumed to be composed of horizontal layers. Resampling of the data to 0.5 ms has been applied so that the NMO–reverse NMO application has no significant effect on the amplitudes of the data set.

In previous large-offset studies, refraction amplitudes were adjusted to the initial smooth forward model (Brenders and Pratt, 2007a) because of the attenuation issue. In our simple case, however, this method is not necessary and would also

destroy the relative variation of the refraction amplitudes along the profile, which would result in a loss of information.

STARTING MODEL

Seismic source

Once the raw data have been processed to correspond to the 2D acoustic code approximation, the next step is to find an accurate initial velocity field in which the modeled first reflection and refraction waves arrive within half a cycle of the observed data at the lowest frequency available (i.e., 8 Hz). If the half-wavelength criterion is not respected, cycle skipping will occur, and the waveform inversion will converge toward a local minimum. To obtain the initial forward model, a source wavelet is necessary. Previous studies using frequency-domain waveform tomography (Pratt, 1999) usually estimate the source wavelet by solving a linear inverse problem progressively updating the source to fit the data from an initial estimation. This approach assumes that the velocity model used for the source estimation produces synthetic data that match reasonably well the field data used for the source inversion. As the subsurface reflectivity is not present in the initial velocity model, we cannot perform the source inversion. Consequently, we use a synthetic source modeled for the 32-air-gun, 4258-cubic-inch (70-L) array geometry used during the acquisition (Figure 3). Our tests show that the modeled wavelet has practically the same frequency spectrum as the data (see Figure 3b). We also know that there were no gun malfunctions or pressure variations during the

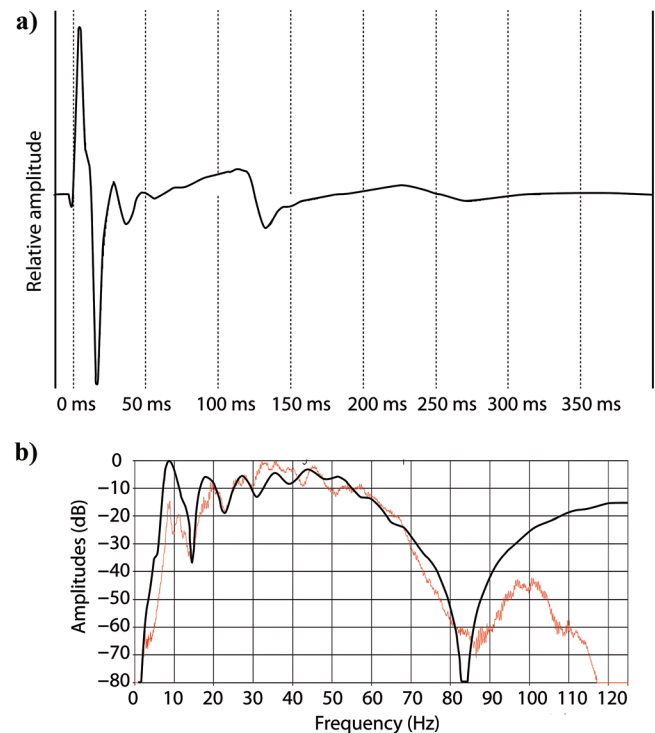


Figure 3. (a) Modeled source wavelet using Gundalf software. (b) Frequency spectrums of the field data (red) and of the modeled source wavelet (black).

acquisition, which yields constant signal strength from shot to shot.

NMO, depth migration, and traveltimes tomography starting velocity models

The synthetic data computed using the velocity fields from NMO stack and prestack depth migration fail to produce refracted arrival times within half a cycle of the observed data. The velocity models are similar and too slow (Figure 4a), and therefore, the modeled arrivals are too late (Figure 5a).

Starting with the depth migration velocity field, we next use traveltimes tomography to obtain a new velocity field (Figure 4b), modeling only the refracted arrivals at far offset. We use the FAST code (Zelt and Barton, 1998), which has been modified to account for direct waves arriving before the refracted arrivals. For this situation, virtual sources are placed at the seafloor to divide the problem in two parts and bypass the direct paths in the water column (Canales et al., 2008). The resulting velocity field now qualifies as a starting model for waveform tomography, as the modeled arrivals now respect the half-cycle criterion (Figure 5b). The new starting model includes a velocity increase relative to the initial model of 0–50 m/s in the top 1 km below the seafloor and 50–150 m/s at depths (between 1 and 1.5 km below seafloor) where the refracted rays turn.

INVERSION STRATEGY

Frequency-domain inversion

We use the frequency-domain waveform tomography approach of Pratt and Worthington (1990) and Pratt (1999)

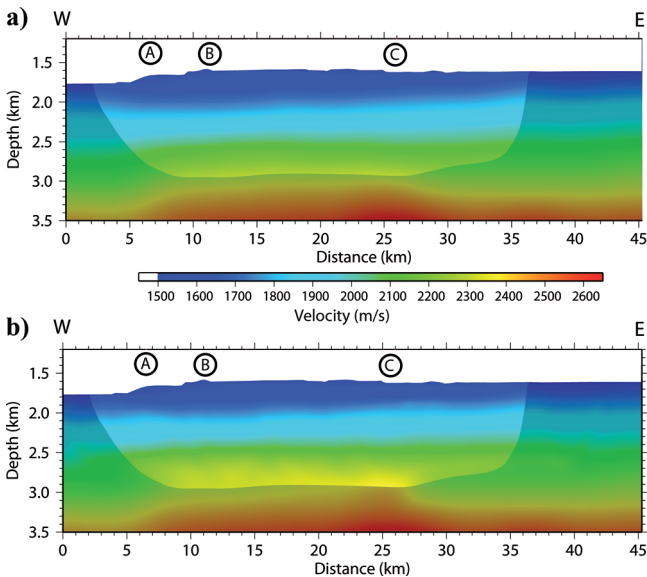


Figure 4. Starting velocity models for the full waveform tomography. (a) Smoothed prestack depth migration velocity field for line 5300 and (b) the starting velocity model obtained after traveltimes tomography. Traveltimes tomography updates the velocity only in the highlighted area, indicating limited depth penetration as constrained by the 9-km-long streamer. Positions A, B, and C approximately correspond to shot gathers displayed in Figure 5.

following the method briefly described in the section about waveform tomography. This method is computationally efficient because the data are manipulated in frequency domain and are used progressively from lower to higher frequencies. This incremental frequency strategy also helps overcome the nonlinearity of the wavefield inversion. The frequency bandwidth is limited by the lowest useable signal frequency in the data set (8 Hz) and also by the size of the forward model grid. The finite-difference forward-model code needs four nodes per spatial wavelength for a 95% accuracy (Jo et al., 1996; Brenders and Pratt, 2007a). For the inversion to run within a reasonable computing time (i.e., <24 h with the decimated data set), we limit our velocity grid size to a 3020×333 dimension, which corresponds to a 15-m spacing (45×5 km). With the lowest velocity being 1500 m/s, four nodes correspond to a $1500 \text{ m/s}/60 \text{ m} = 25$ Hz maximum frequency. Because structures are seen through different incident angles, one frequency illuminates a range of spatial wavenumbers (Sirgue and Pratt, 2004), which means that a small number of frequencies cover a continuous range of spatial wavenumbers. With a 9-km streamer, this “efficient waveform tomography” strategy (Sirgue and Pratt, 2004; Brenders and Pratt, 2007b) would result in the use of only four frequencies in our 8- to 25-Hz data. However, real data are noisy, and although the Ion-GXT data set has a good signal-to-noise ratio, more frequencies are necessary to create some overlap in the spatial wavenumber coverage and avoid noise artifacts. In our case, nine frequencies are used from 8 to 24 Hz with a 2 = Hz step. Fewer frequencies could potentially be used, but to our knowledge, there is no clear rule on how many are needed to counter the effect of noise, so we prefer to be conservative.

Iteration strategy

Once frequencies have been selected, the number of iterations per frequency must be determined. The general behavior of the cost function in terms of iterations for the nine frequencies is given in Figure 6a. For the three first frequencies (8–12 Hz), most of the misfit reduction occurs by three iterations, with the remaining iterations producing a more gentle decrease of the cost function. The three “middle” frequencies (14–18 Hz) follow more or less the same pattern but with a more moderate total decrease of the cost function after six iterations, perhaps because of the poor signal-to-noise ratio at those frequencies (Figure 2). The three highest frequencies show a more linear decrease, and additional iterations might be required if we base our inversion strategy purely on the cost function reduction.

We show in Figure 7 the three iterations per frequency velocity field and the six iterations per frequency velocity field. The difference is clearly related to reflectivity. The six iterations per frequency inversion has minimal residuals and looks closer to a depth-migrated image. However, our goal in this study is not to obtain a reflectivity image from the data but to model the background velocity field. The only difference between the iterations in terms of velocity imaging is the increased amplitude of reflectors, without any significant change in the low-wavenumber background velocity field (see 1D profiles in Figure 7c). In addition, the six-iterations result may be affected by the modeling methodology, in which we do not invert for the density and the reflectivity is only a function of velocity. The density input in the inversion is increasing with depth following a simple

porosity law. It is not updated. This can lead to an overestimation of velocity changes that are needed to match the reflection amplitudes. Therefore, we stop after three iterations per frequency because the low-wavenumber background velocity (such as the low velocity at around 2-km depth discussed in the next section) is successfully retrieved.

In an effort to further limit the weight of reflections in the inversion, we also ignore the first 160 near-offset traces of each shot gather and only consider the 200 receivers from offsets of 4–9 km. The weight of near-offset reflections is high in the inversion gradient, although they carry little low-wavenumber background velocity information. The high amplitudes of the near-offset sea-bottom reflection are also unlikely to be correctly modeled by the 2D acoustic code (Hicks and Pratt, 2001). The difference between a velocity field obtained with all the receivers and a velocity field obtained with far-offset receivers is minimal (Figure 8). Moreover, with inversions using all the receivers, a few diverging iterations appear and slow the inversion, which does not happen when using only the far-offset receivers. This effect may be due to anisotropy with low-incidence reflection rays travelling slower than higher-incidence wide-angle reflections or refractions as a result of horizontal layering with embedded low velocities (Figure 7 and next sections).

Full versus decimated data set

It is useful to compare the behavior of the cost functions for high frequencies with those in the decimated inversion (every third shot). Figure 6b shows a smaller reduction of the cost functions for frequencies higher than 14 Hz. For an average 2000-m/s velocity, 14 Hz illuminates wavelengths around 150 m, which is precisely the distance between the shots. In this case, horizontal smoothing of the inversion gradient filters wavelengths smaller than 150 m so that “along-wave-path” artifacts are minimized (see Figure 9). This can explain why the inversion is less efficient for these high frequencies. In the nondecimated, full data-set inversion (Figure 6a), the behavior of the 22- and 24-Hz cost functions can be interpreted as the result of the 50-m smoothing of the gradient we apply in this case. This shows that even with a finer grid, inversion of frequencies far beyond 25 Hz would not be useful.

While the decimated inversion is smoothed and still shows along-wave-path artifacts (Figure 9), those are moderate. In this case of a very simple geological setting, it is hard to justify the high computational cost of the full data-set inversion. We are using a sequential code and the full data-set inversion can take up to a week. The three iterations per frequency inversion of the decimated data set takes a bit less than 24 h to run, which is much more efficient.

The results of the phase and amplitude inversion for line 5300 are shown in Figures 10 and 11. The results for line 1400 are displayed in

Figure 12. All these figures show three iterations per frequency inversion. The velocities at the crossing between the two lines are in very good agreement (Figure 12). The next section will discuss those results in terms of comparison with the migrated section and the validity of the acoustic approximation in this specific sedimentary environment.

DISCUSSION

Interpretation of the results and comparison with the migrated section

Line 5300

Figure 10 shows the result of our inversion for line 5300 derived using 9 frequencies and a total of 27 iterations. Several significant features are now derived that did not exist in the initial smooth velocity model from traveltimes tomography. First, a velocity contrast appears around 2-km depth. On the migrated section (Figure 10), it clearly corresponds to the bottom-simulating reflector (BSR) that is visible at the same depth between 5 and 8 km. A BSR marks the thermal and pressure stability limit of gas hydrates, which can trap some free gas underneath. As a result, a velocity inversion is expected to follow the seafloor

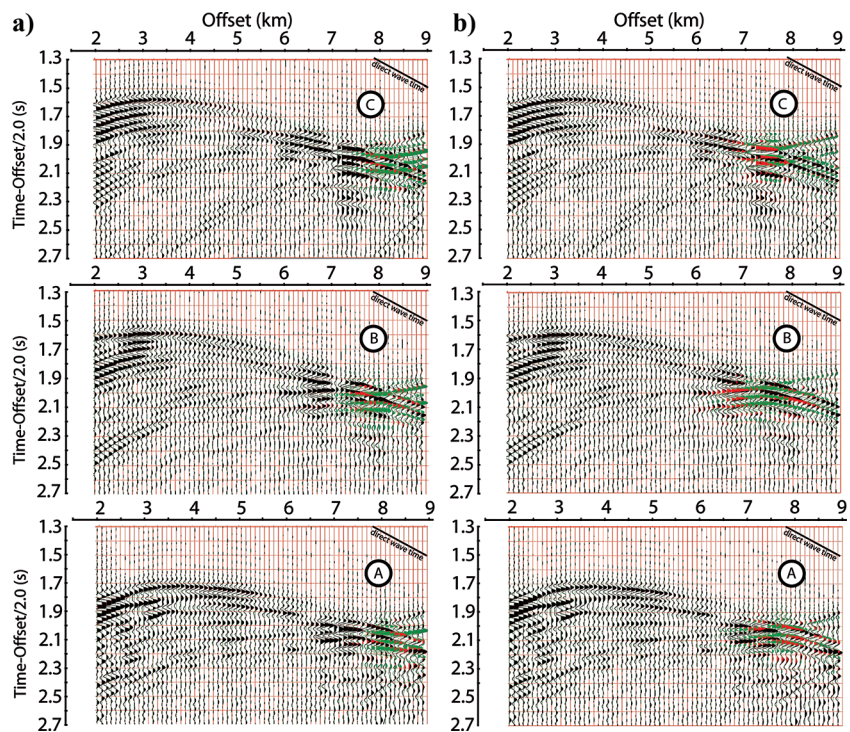


Figure 5. Shot gathers corresponding to positions A, B, and C in Figure 4. The wavefields are displayed for every fourth trace with a 2-km/s reduced velocity. Real data are in black, and the synthetic data are in green; common areas are in red, even when the phases are wrong. (a) The modeled refractions arrive too late in the migration velocity case. (b) For clarity and homogeneity with the later figures, we display an 8- to 25-Hz wavefield, and although the match with the far-offset refraction arrival is not perfect at 25 Hz for shots A and B, the model clearly fits the data within half a cycle at 8 Hz after traveltimes tomography. The seafloor reflection is very weak in the models because the velocities are smooth, which makes the part of the refraction event arriving after the seafloor more visible.

topography because hydrates have the effect of increasing velocity (Hyndman and Spence, 1992; Minshull et al., 1994; Leblanc et al., 2007; Rossi et al., 2007), whereas gas lowers it. This is exactly what happens between 5 and 8 km of line 5300, where the velocity drops almost by 200 m/s. Figure 13 shows a good agreement between our velocities and those previously obtained with ocean bottom seismometer (OBS) data (Leblanc et al., 2007) in the same area. Of particular interest is that this low-velocity layer continues eastward, where the prestack depth migrated image does not show a clear BSR. The contrast between those two velocity zones gradually decreases toward the east (compare velocity profiles A, B, and C in Figure 10), but it is still detected by the waveform tomography image. The largest polygonal fault in the migrated section is also imaged (Figure 10) in our waveform inversion velocity field, which shows the high horizontal resolution of the image. Polygonal fault systems are composed of normal faults organized in polygonal networks (in plan view) (Cartwright and Dewhurst, 1998). They are well developed in the area surrounding the NovaSpan profiles (Hansen et al., 2004). Although still under debate (Cartwright et al., 2003), their origin can be related to diverse and sometimes combined mechanisms like gravity collapse, fluid pressure, sediment flexure, and compaction (Hansen et al., 2004).

Deeper information can also be extracted from this new velocity field. The gently dipping reflector around 2.4-km depth acts as the ~2000-m/s limit, and the sediments below it have a much faster velocity than in the migration velocity field. This is

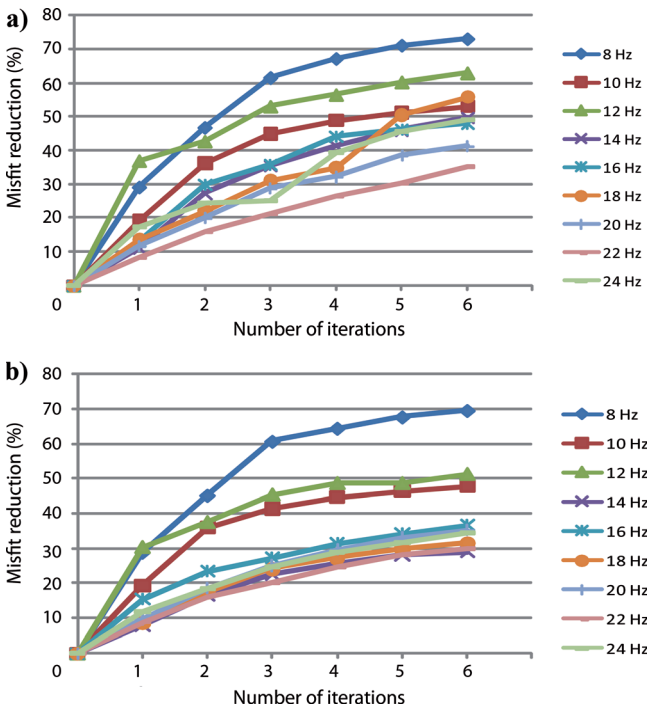


Figure 6. Reduction of the misfit as a function of the number of iterations for the nine frequencies used in the inversion. (a) Full data-set inversion for line 5300 (691 shots) with 50-m horizontal and vertical smoothing. (b) Decimated line 5300 (231 shots) with 150-m horizontal smoothing and 50-m vertical smoothing of the gradient.

the depth where the refracted rays turn. In the western half of the profile, this dipping reflector has a strong amplitude. In the waveform tomography image, it corresponds to a low-velocity zone above it (see velocity profile B, LVZ in Figure 10). The 2.9-km-deep discontinuous reflector is imaged as a low-velocity boundary, except toward its eastern extremity, where it is imaged as a high velocity (velocity profile C in Figure 10). In general, lower velocities are present to the west of the profile, and shallower, higher velocities emerge to the east.

On the shot gathers (Figure 11), this lateral evolution is visible with a clear, long-refraction event for the western shot gathers (corresponding to profile A) and a later refraction event, with slightly higher velocity (deeper, more-compacted high-velocity sediments?) for the eastern shot gathers (corresponding to profiles B and C). Lower-refraction amplitudes on shot gather B correspond to the low-velocity region (Figure 10) just above the 2.4-km-deep high-amplitude reflector. The general trend of the crossover between reflection and refraction phases also varies laterally and is quite closely matched by the inversion. Contrary

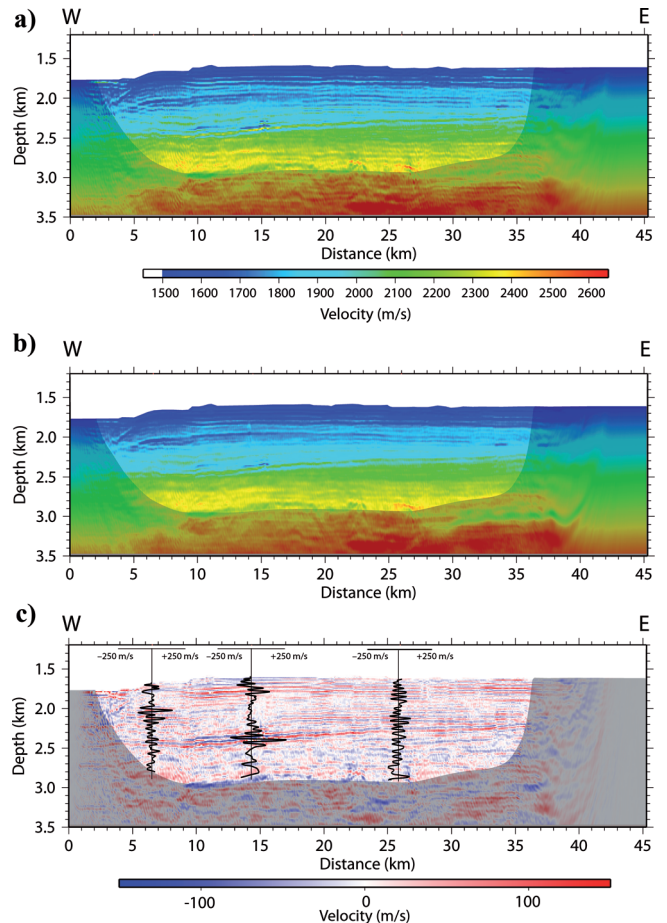


Figure 7. Phase plus amplitude inversion result for the decimated line 5300. (a) Six iterations per frequency. (b) Three iterations per frequency. (c) Difference field A-B. One-dimensional profiles of the difference field are superimposed at three selected locations. The profiles show similar low wavenumbers in velocity fields (a) and (b). Nine frequencies (range of 8–24 Hz with a 2-Hz step) were used.

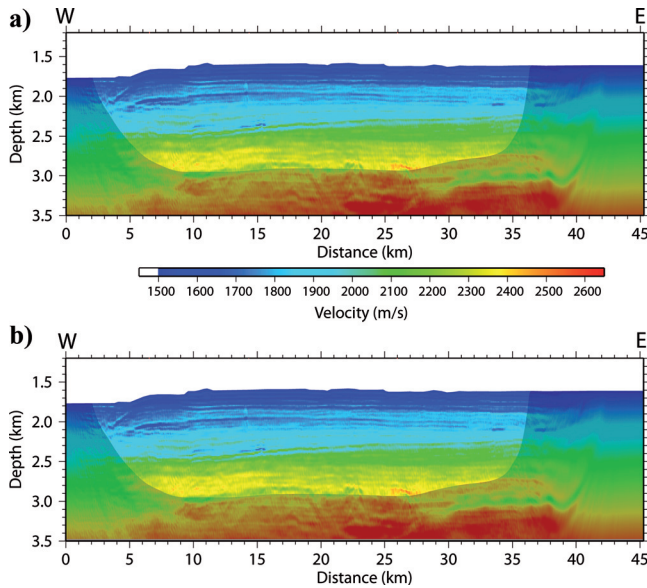


Figure 8. Phase-plus-amplitude inversion result for the decimated line 5300. (a) With all receivers included. (b) With only 200 far-offset receivers. Nine frequencies (range of 8–24 Hz with a 2-Hz step) were used.

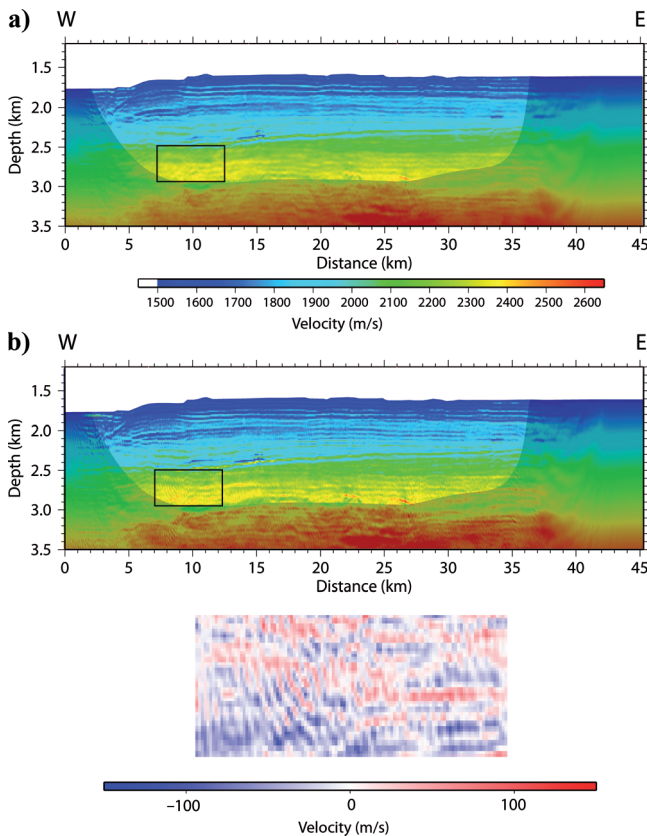


Figure 9. Phase-plus-amplitude inversion results (a) for the full data set of line 5300 and (b) for the decimated line 5300. (c) Six iterations per frequency are used to emphasize the “along-wave-path” artifacts (difference field (a-b) in the framed section of the profile). Nine frequencies (range of 8–24 Hz with a 2-Hz step) were used.

to first-arrival traveltome tomography, waveform tomography is able to use refraction waves even when they are not the first arrival. The extent of the available refraction information can be seen in synthetic data produced using the starting velocity (green wiggles in Figure 5).

Line 1400

Figure 12 shows the result of the same inversion strategy for the crossing profile 1400. Fewer shots are available, but the crossing point with line 5300 is well imaged, and the velocity at that position can be compared on both profiles. The two profiles show nearly identical velocity variations. The high- and low-velocity contrast corresponding to the gas-hydrates stability limit is also present toward the landward part of the profile, with the low-velocity layer gradually diminishing seaward. Some reflectors cross the high-velocity layer between 26 and 35 km, which indicates that this high velocity follows the seafloor and not the lithology (Figure 12). The 2.3-km-deep reflector is also the ~2000-m/s isovelocity limit on this profile. Finally, the 2.9-km-deep reflector is also related to a high velocity at the crossing point, although this same reflector corresponds to a lower velocity just farther north. Some dipping artifacts are visible on this profile because the depth of the turning waves varies laterally as a consequence of the nonflat bathymetry (see stars in Figure 12).

Phase and amplitude inversions and the applicability of acoustic waveform tomography to long-streamer MCS data

Using long-streamer data means using reflection arrivals near or beyond the critical angle, with potentially important P- to S-wave conversions at far offsets. The acoustic code we use does not take into account the energy lost by S-wave conversions, and the use of the amplitude information could be affected. It is thus important to check that our results are not significantly impacted by this limitation.

To assess the effect of S-wave conversions in our specific marine sedimentary environment, we compute two synthetic shot gathers (Figure 14) in a 1D velocity model corresponding to profile B (Figure 10). This profile has been chosen because two velocity inversions are present, which represent the most complex features in the section. The first synthetic shot gather is a purely acoustic response, whereas the second is the acoustic record (the receivers are in the water) including P-S and S-P conversions (Fuchs and Mueller, 1971; Kennett, 1974). While we acknowledge that lateral variations of the velocity field could impact P-S conversions, in our case, as already discussed, we are very close to a 1D situation. The nature of the sediments (mudstones and claystones) and the low seafloor density (1680 kg/m³) are compatible with the use of high Poisson’s ratios (0.49 at the seafloor to 0.41 at 1-km depth [Hamilton, 1979]) to determine the S-wave velocity used in the 1D forward model. The difference between the two synthetic shots (Figure 14) is not significant and establishes the applicability of the acoustic waveform tomography to this data set, corresponding to a smooth S-wave velocity field (Barnes and Charara, 2009).

When these conditions are not met, this type of test is very useful to determine what part of the wavefield cannot be used for phase-plus-amplitude inversion. In general, first refraction

Figure 10. Waveform tomography velocity model for GXT line 5300 (a) using nine frequencies (range of 8–24 Hz with a 2-Hz step). (b) The prestack depth-migrated reflection image for comparison. The BSR is visible at 2-km depth between distances of 5–8 km. Red curves show velocity versus depth at three specific locations (A, B, and C). These locations correspond to the shot gathers on Figure 11. Position C is the crossing point with profile 1400 (see Figure 12). Shaded areas are not covered by the refracted rays recorded on the 9-km-long streamer. G.H. indicates the gas-hydrates layer (high velocity) below which low-velocity free gas is trapped. The high amplitudes at 2.4-km depth on the prestack depth-migration profile correspond to the low-velocity zone (LVZ) above the reflector in the velocity model.

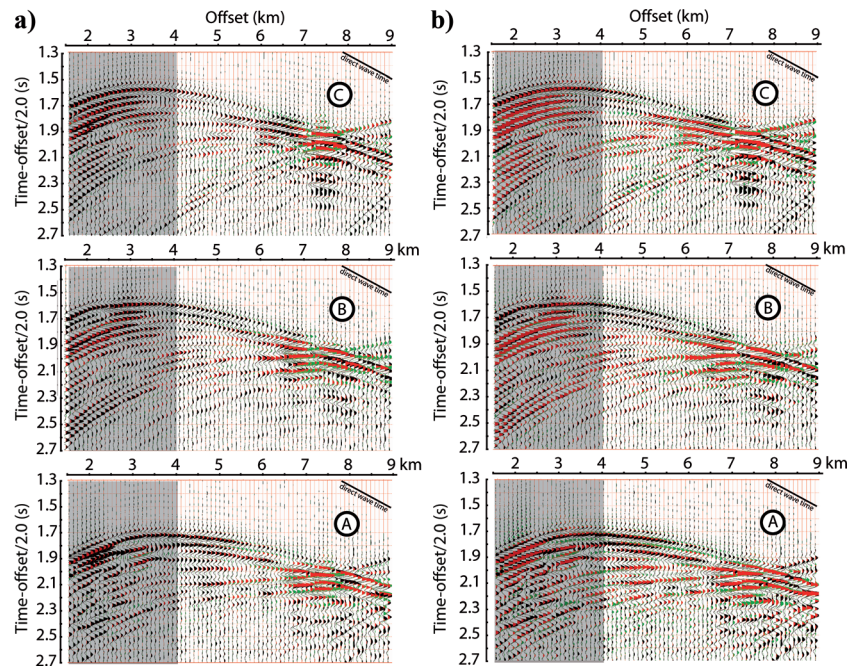
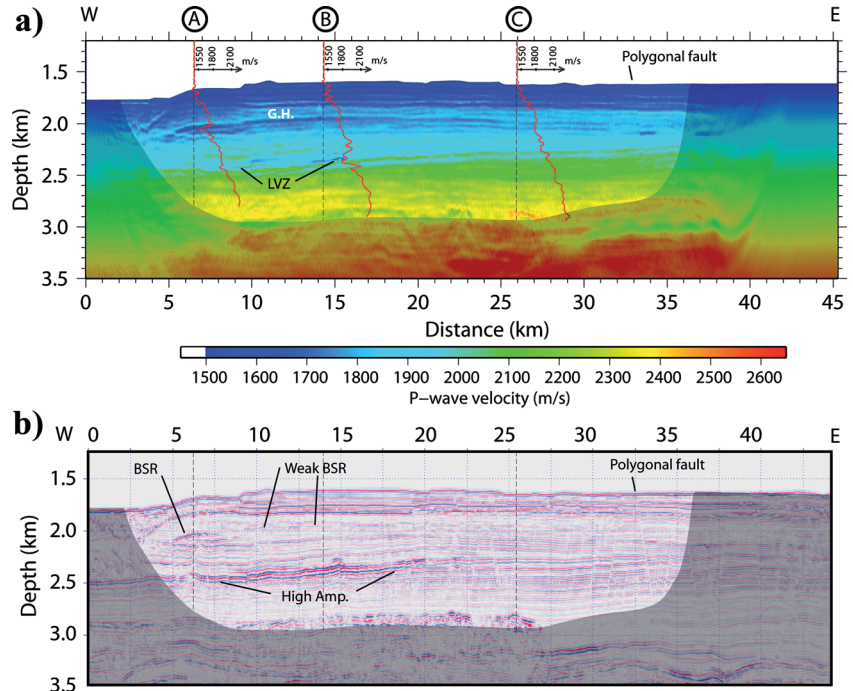


Figure 11. Observed (black) and modeled (green) shot gathers ($f_{\max} = 25$ Hz). The refracted waves on these shot gathers turn approximately at positions A, B, and C in Figure 10. Areas where the modeled seismograms match the recorded ones are shown in red. The wavefields are displayed with a 2-km/s reduced velocity. Shaded receivers for nearest offsets (0–4 km) are not used in the inversion. Only every fourth trace is displayed. Shot gathers are modeled (a) in the phase-only waveform velocity model (Figure 15a) and (b) in the phase-plus-amplitude waveform velocity model (Figures 10 and 15b). Notice how even the phases of the refracted arrivals at far offset are improved by the addition of the amplitudes in the inversion (shots A and B).

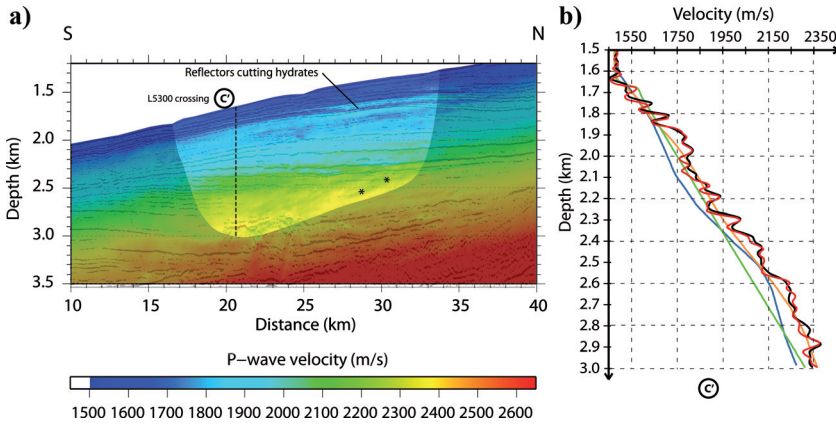


Figure 12. (a) Waveform tomography velocity model for GXT line 1400 using nine frequencies (range of 8–24 Hz with a 2-Hz step) superimposed on the prestack depth-migrated reflection image. Shaded areas are not covered by the refracted rays recorded on the 9-km-long streamer. Dipping artifacts are visible between 25 and 35 km just above the shaded area limit (stars). (b) Velocity at the crossing point C with line 5300 (Figure 10). The NMO (blue), migration (green), traveltime tomography (orange), and waveform tomography velocities for lines 1400 (black) and 5300 (red) are displayed. Note the excellent agreement between the waveform inversion models at the crossing point.

arrivals have a small incident angle and thus can often be used if there are no strong lateral variations of attenuation, which is a potential problem with OBS data sets (Bleibinhaus et al., 2007, 2009) because long profiles may cross very different geological terrains. Gas hydrates and free-gas presence can imply a large change in attenuation (Guerin and Goldberg, 2002; Rossi et al., 2007; Madrussani et al., 2010). However, in our case, the con-

centration of free gas and hydrates in the area calculated by Leblanc et al. (2007) and based on a model by Helgerud et al. (1999) are only 2%–6% and <1%, respectively. This implies only moderate attenuation without any sudden lateral change because the amount of free gas is only slowly evolving and the gas-hydrate layer shows almost constant velocity along the profiles. The low concentration and smooth lateral evolution of gas hydrates and free gas do not lead to a significant lateral change in attenuation along the profiles, as earlier assumed.

Figure 15 shows the phase-only inversion of line 5300, with all other parameters unchanged. Comparison with the phase-plus-amplitude inversion shows a large improvement of the result relative to phase only, which is another indication of the validity of the acoustic approximation in our specific case. Inversions of data sets with significant elastic effects (Bednar et al., 2007; Shin et al., 2007) can lead to a better result of the phase-only tomography when compared to the phase-plus-amplitude tomography, which is clearly not our case. We are confident that unmodeled parameters (small lateral variations, higher S-wave velocity contrasts at

the BSR) do not significantly impact the validity of the acoustic approximation. Comparing the synthetic wavefields in the “phase” and “phase-plus-amplitude” waveform-inverted velocities (Figure 11) shows a much better fit of the refraction event when using the amplitude information. This improvement of the modeled wavefield corresponds to a clear improvement of the velocity contrast below the hydrate layer (see difference field in Figure 15) and a much more detailed image in general.

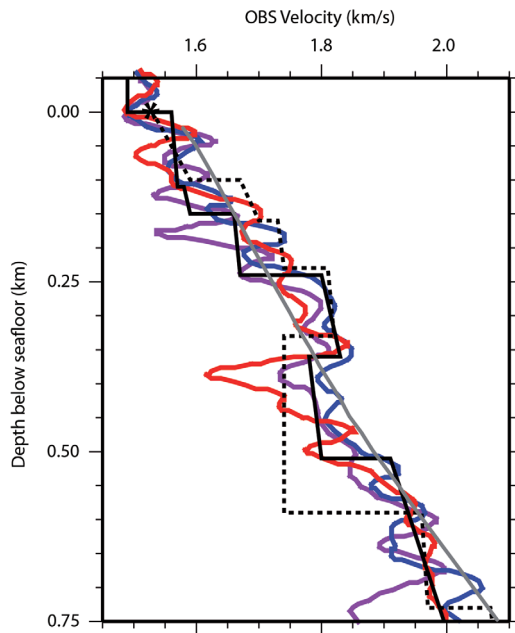


Figure 13. OBS velocities from Leblanc et al. (2007) (solid and dashed black lines) superimposed with velocities (A, red; B, purple; C, blue) of Figure 10. The gray line is a reference velocity considering sediment compaction (see details in Leblanc et al., 2007).

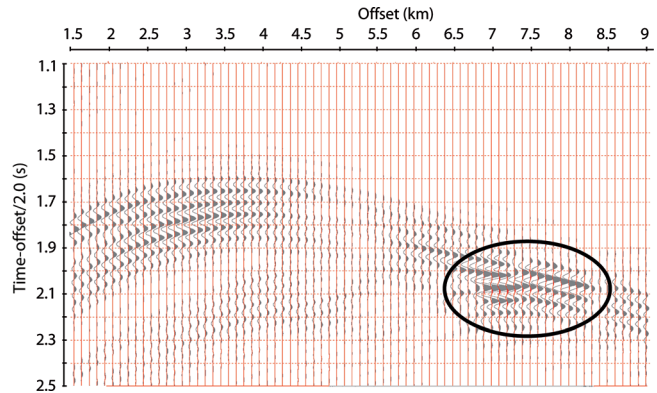


Figure 14. Acoustic synthetic shot gather (gray) computed in a 1D velocity model representative of profile B in Figure 10. The red wiggles are the difference field between the purely acoustic case and the acoustic part of the full seismic case including S-wave conversion at the horizontal layer interfaces. The part of the wavefield where the difference is noticeable, but not significant, is circled. The critical angle for the seafloor is 74° , using velocities and densities derived from cores, corresponding to an offset of 11 km.

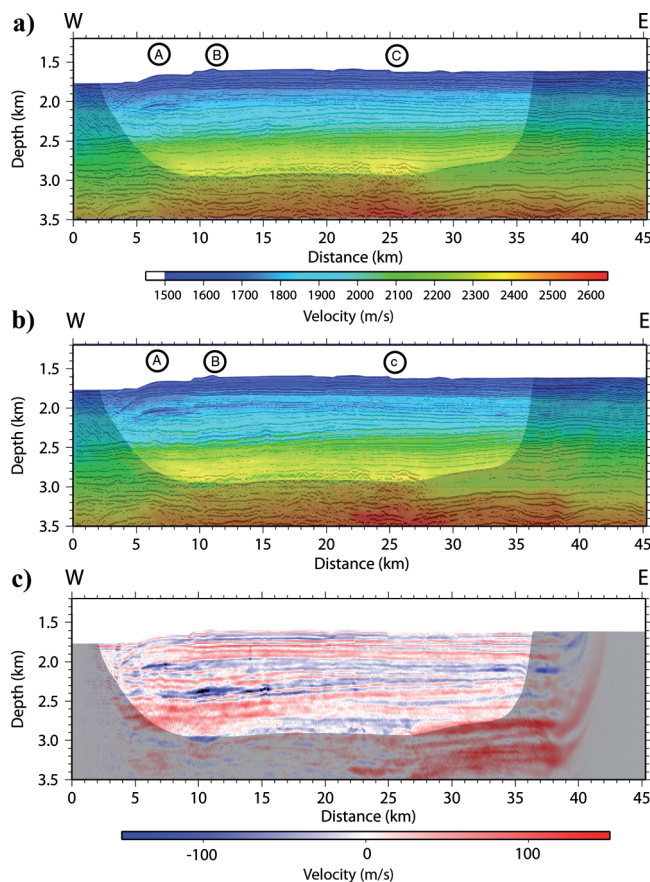


Figure 15. Velocity models after (a) phase-only inversion and (b) phase-plus-amplitude inversion. The prestack depth migration profile is superimposed. (a) The difference field between the two results of the inversions emphasizes how crucial the amplitude information is to retrieve the velocity inversion at the weak BSR. Positions A, B, and C approximately correspond to shot gathers displayed in Figure 11.

CONCLUSIONS

Acoustic waveform tomography applied to MCS data is a promising imaging method when used in a suitable environment. The relatively high starting frequency (~ 8 Hz) and the limited weight of the refractions in the data set used in this study require a good starting velocity model for a successful inversion. A more complex environment, with all other parameters unchanged, could potentially limit the ability to determine a successful starting velocity model because intermediate wavelength would be missing. Further efforts are also needed to study the effect of anisotropy between near-offset and far-offset receivers. The addition of a more-accurate density model would allow for extraction of more-realistic velocity contrasts for reflectors. This would help resolve the trade-off between further reducing the inversion residuals and exaggerating the reflectivity-related velocity contrasts.

This study confirms that using long-streamer data does not necessarily imply strong elastic effects if the S-wave velocity is smoothly increasing with depth. Using a longer streamer (e.g., 15 km) or modeling structures in shallower water depths could help to extend the depth of the inversion, although in the second

case the multiple reflections would interfere. Joint inversion of MCS and OBS data would then be the most robust solution to obtain a refraction-based high-resolution velocity model at all depths imaged by the MCS reflection method. OBS data, through the use of lower frequencies and more robust traveltimes inversions, could also help cover the intermediate wavenumbers that may be missed by using MCS data with high starting frequencies.

In the meantime, the use of MCS acoustic waveform tomography appears to be adapted best to studies of shallow sediment, such as the characterization of gas-hydrate structures. The high-resolution background velocity field aids the interpretation of a low-amplitude reflector as the continuation of a strong and well-defined BSR. For deeper reflectors, it associates the main sedimentary units to characteristic velocities and detects velocity inversions down to the depth limit of the turning waves (Figure 10).

ACKNOWLEDGMENTS

We thank Ion-GXT for use of the NovaSPAN seismic data set. David Mosher (Geological Survey of Canada, Atlantic Division) kindly allowed us to use the Gundalf© source modeling software. We thank G. Pratt for use of his code. We also thank Mathias Alerini, Giuliana Rossi, and two anonymous reviewers for their very constructive reviews. Velocity figures were prepared with GMT software (Wessel and Smith, 1995) and shot gathers were displayed with Paradigm Focus© software.

REFERENCES

- Barnes, C., and M. Charara, 2009, The domain of applicability of acoustic full-waveform inversion for marine seismic data: *Geophysics*, **74**, no. 6, WCC91–WCC103, doi: 10.1190/1.3250269.
- Bednar, J. B., C. Shin, and S. Pyun, 2007, Comparison of waveform inversion, Part 2: Phase approach: *Geophysical Prospecting*, **55**, 465–475.
- Bleibinhaus, F., J. A. Hole, T. Ryberg, and G. S. Guys, 2007, Structure of the California Coast Ranges and San Andreas Fault at SAFOD from seismic waveform inversion and reflection imaging: *Journal of Geophysical Research*, **112**, B06315, doi: 10.1029/2006JB004611.
- Bleibinhaus, F., R. W. Lester, and J. A. Hole, 2009, Applying waveform tomography to wide-angle seismic surveys: *Tectonophysics*, **472**, 238–248, doi: 10.1016/j.tecto.2008.08.023.
- Brenders, A. J., and R. G. Pratt, 2007a, Full waveform tomography for lithospheric imaging: Results from a blind test in a realistic crustal model: *Geophysical Journal International*, **168**, 133–151, doi: 10.1111/j.1365-246X.2006.03156.x.
- Brenders, A. J., and R. G. Pratt, 2007b, Efficient waveform tomography for lithospheric imaging: Implications for realistic, two-dimensional acquisition geometries and low-frequency data: *Geophysical Journal International*, **168**, 152–170, doi: 10.1111/j.1365-246X.2006.03096.x.
- Brenders, A. J., and R. G. Pratt, 2007c, Waveform tomography of marine seismic data: What can limited offset offer?: 75th Annual International Meeting, SEG, Expanded Abstracts, 3024–3029.
- Brossier, R., S. Operto, and J. Virieux, 2010, Which data residual norm for robust elastic frequency-domain full waveform inversion?: *Geophysics*, **75**, no. 3 R37–R46, doi: 10.1190/1.3379323.
- Canales, J. P., B. E. Tuelholke, M. Xu, J. A. Collins, and D. DuBois, 2008, Seismic evidence for large-scale compositional heterogeneity of oceanic core complexes: *Geochemistry, Geophysics, Geosystems*, **9**, Q08002, doi: 10.1029/2008GC002009.
- Cartwright, J.A., and D. N. Dewhurst, 1998, Layer-bound compaction faults in fine-grained sediments: *Geological Society of America Bulletin*, **110**, 1242–1257.
- Cartwright, J., D. James, and A. Bolton, 2003, The genesis of polygonal fault systems: A review, in P. Van renstbergen, R. R. Hillis, A. J. Maltman, and C. K. Morley, eds., *Subsurface sediment mobilization: Geological Society Special Publication 216*, 223–243.
- Dessa, J.-X., S. Operto, S. Kodaira, A. Nakanishi, G. Pascal, J. Virieux, and Y. Kaneda, 2004, Multiscale seismic imaging of the eastern Nankai

- trough by full waveform inversion: *Geophysical Research Letters*, **31**, L18606, doi: 10.1029/2004GL020453.
- Fuchs, K., and G. Mueller, 1971, Computation of synthetic seismograms by the reflectivity method and comparison with observations: *Geophysical Journal of the Royal Astronomical Society*, **23**, 417–433.
- Guerin, G., and D. Goldberg, 2002, Sonic waveform attenuation in gas hydrate-bearing sediments from the Mallik 2L-38 research well, Mackenzie Delta, Canada: *Journal of Geophysical Research*, **107**, no. B5, 2088, doi: 10.1029/2001JB000556.
- Hamilton, E. L., 1979, V_p/V_s and Poisson's ratios in marine sediments and rocks: *Journal of the Acoustical Society of America*, **66**, 1093–1101.
- Hansen, D. M., J. W. Shimeld, M. A. Williamson, and H. Lykke-Andersen, 2004, Development of a major polygonal fault system in Upper Cretaceous chalk and Cenozoic mudrocks of the Sable Subbasin, Canadian Atlantic margin: *Marine and Petroleum Geology*, **21**, 1205–1219, doi: 10.1016/j.marpetgeo.2004.07.004.
- Helgerud, M. B., J. Dvorkin, A. Nur, A. Sakai, and T. Collett, 1999, Elastic-wave velocity in marine sediments with gas hydrates: Effective medium modeling: *Geophysical Research Letters*, **26**, 2021–2024.
- Hicks, G., and R. G. Pratt, 2001, Reflection waveform inversion using local descent methods: Estimating attenuation and velocity over a gas sand deposit: *Geophysics*, **66**, 770–780.
- Hyndman, R. D., and G. D. Spence, 1992, A seismic study of methane hydrate marine bottom simulating reflectors: *Journal of Geophysical Research*, **97**, 6683–6698.
- Jannane, M., W. Beydoun, E. Crase, D. Cao, Z. Koren, E. Landa, M. Mendes, A. Pica, M. Noble, G. Roeth, S. Singh, R. Snieder, A. Tarantola, D. Trezeguet, and M. Xie, 1989, Wavelengths of earth structures that can be resolved from seismic-reflection data: *Geophysics*, **54**, 906–910.
- Jo, C. H., C. S. Shin, and J. H. Su, 1996, An optimal 9-point, finite-difference, frequency-space, 2-D scalar wave extrapolator: *Geophysics*, **61**, 529–537.
- Kennett, B. L. N., 1974, Reflections, rays and reverberations: *Bulletin of the Seismological Society of America*, **64**, 1685–1696.
- Lailly, P., 1983, The seismic inverse problem as a sequence of before stack migrations, in J. B. Bednar, R. Redner, E. Robinson, and A. Weglein, eds., *Conference on inverse scattering: Theory and application: Society for Industrial and Applied Mathematics*, 206–220.
- LeBlanc, C., K. Loudon, and D. Mosher, 2007, Gas hydrates off eastern Canada: Velocity models from wide-angle seismic profiles on the Scotian Slope: *Marine and Petroleum Geology*, **24**, 321–335, doi: 10.1016/j.marpetgeo.2006.05.008.
- Madrussani, G., G. Rossi, and A. Camerlenghi, 2010, Gas hydrates, free gas distribution and fault pattern on the west Svalbard continental margin: *Geophysical Journal International*, **180**, 666–684, doi: 10.1111/j.1365-246X.2009.04425.x.
- Minshull, T. A., S. C. Singh, and G. K. Westbrook, 1994, Seismic velocity structure at a gas hydrate reflector, offshore western Colombia, from full-wave-form inversion: *Journal of Geophysical Research*, **99**, 4715–4734.
- Mosher, D.C., K. Moran, and R. N. Hiscott, 1994, Late Quaternary sediment, sediment mass-flow processes and slope stability on the Scotian Slope: *Sedimentology*, **41**, 1039–1061.
- Newman, K. R., M. R. Nedimovic, J. P. Canales, and S. M. Carbotte, 2011, Evolution of seismic layer 2B across the Juan de Fuca Ridge from hydrophone streamer 2D traveltine tomography: *Geochemistry, Geophysics, Geosystems*, **12**, doi: 10.1029/2010GC003462.
- Operto, S., C. Ravaut, L. Improta, J. Virieux, A. Herrero, and P. Dell'Aversana, 2004, Quantitative imaging of complex structures from dense wide-aperture seismic data by multiscale traveltine and waveform inversions: A case study: *Geophysical Prospecting*, **52**, 625–651.
- Operto, S., J. Virieux, J. X. Dessa, and G. Pascal, 2006, Crustal seismic imaging from multifold ocean bottom seismometer data by frequency domain full waveform tomography: Application to the eastern Nankai trough: *Journal of Geophysical Research*, **111**, B09306, doi: 10.1029/2005JB003835.
- Piper, D. J. W., and W. R. Normark, 1989, Late Cenozoic sea-level changes and the onset of glaciation: Impact on continental slope progradation off eastern Canada: *Marine Petroleum and Geology*, **6**, 336–348.
- Pratt, R. G., 1999, Seismic waveform inversion in the frequency domain; Part 1, Theory and verification in a physical scale model: *Geophysics*, **64**, 888–901.
- Pratt, R. G., C. Shin, and G. Hicks, 1998, Gauss-Newton and full Newton methods in frequency-space seismic waveform inversion: *Geophysical Journal International*, **133**, 341–362.
- Pratt, R. G., and M. H. Worthington, 1990, Inverse theory applied to multi-source cross-hole tomography. Part I: Acoustic wave-equation method: *Geophysical Prospecting*, **38**, 287–310.
- Ravaut, C., S. Operto, L. Improta, J. Virieux, A. Herrero, and P. Dell'Aversana, 2004, Multiscale imaging of complex structures from multifold wide-aperture seismic data by frequency-domain full-waveform tomography: Application to a thrust belt: *Geophysical Journal International*, **159**, 1032–1056, doi: 10.1111/j.1365-246X.2004.02442.x.
- Rossi, G., D. Gei, G. Bohm, G. Madrussani, and J. M. Carcione, 2007, Attenuation tomography: An application to gas-hydrate and free-gas detection: *Geophysical Prospecting*, **55**, 655–669.
- Shin, C., and D.-J. Min, 2006, Waveform inversion using a logarithmic wavefield: *Geophysics*, **71**, No. 3, R31–R42.
- Shin, C., S. Pyun, and J. B. Bednar, 2007, Comparison of waveform inversion, part 1: Conventional wavefield vs logarithmic wavefield: *Geophysical Prospecting*, **55**, 449–464.
- Shipp, R. M., and S. C. Singh, 2002, Two-dimensional full wavefield inversion of wide-aperture marine seismic streamer data: *Geophysical Journal International*, **151**, 325–344.
- Sirgue, L., 2003, Inversion de la forme d'onde dans le domaine fréquentiel de données sismiques grands offsets: Ph.D. thesis, Université: Paris XI.
- Sirgue, L., 2006, The importance of low frequency and large offset in waveform inversion: 68th Conference and Exhibition, EAGE, Extended Abstracts, A037.
- Sirgue, L., and R. G. Pratt, 2004, Efficient waveform inversion and imaging: A strategy for selecting temporal frequencies: *Geophysics*, **60**, 1870–1874, doi: 10.1190/1.1649391.
- Tarantola, A., 1984, Inversion of seismic reflection data in the acoustic approximation: *Geophysics*, **49**, 1259–1266.
- , 1987, Inverse problem theory: Methods for data fitting and parameter estimation: Elsevier Science Publishers.
- Ursin, 1990, Offset-dependent geometrical spreading in a layered medium: *Geophysics*, **55**, 492–496.
- Virieux, J., and S. Operto, 2009, An overview of full-waveform inversion in exploration geophysics: *Geophysics*, **74**, No. 6, WCC1–WCC26, doi: 10.1190/1.3238367.
- Wang, Y., and Y. Rao, 2009, Reflection seismic waveform tomography: *Journal of Geophysical Research*, **114**, B03304, doi: 10.1029/2008JG005916.
- Wessel, P., and W. H. F. Smith, 1995, New version of the Generic Mapping Tool released: *Eos, Transactions of the American Geophysical Union*, **76**, no. 33, 329.
- Williamson, P., B. Wang, B. Bevc, and I. Jones, 2010, Full wave-equation methods for complex imaging challenges: *The Leading Edge*, **29**, 264–268.
- Zelt, C. A., and P. J. Barton, 1998, Three-dimensional seismic refraction tomography: A comparison of two methods applied to data from the Faeroe Basin: *Journal of Geophysical Research*, **103**, 7187–7210.